Image Anal Stereol 2026;45:167-184 doi: 10.5566/ias.3970
Original Research Paper

ESTIMATION OF PORES VIA ARTIFICIAL PORE INTERSECTIONS

IRVING MARTÍNEZ[✉,1], UTE HAHN[2], JENS VINGE NYGAARD[2] AND CATALINA SUÁREZ LONDOÑO[2]

[1]Department of Mathematics, Aarhus University, Aarhus, Denmark, [2]Department of Biochemical Engineering, Aarhus University, Aarhus, Denmark
e-mail: irving915656@gmail.com, ute@math.au.dk, jvn@bce.au.dk, csl@bce.au.dk
(Received March 31, 2026; revised June 26, 2026; accepted June 26, 2026)

ABSTRACT

Pores are ubiquitous in nature and tend to be extremely complex. Watershed is standard imaging tool in many applications for pore estimation because of its efficiency to capture closed pores. However, oftentimes materials do not have clearly delineated borders, making it difficult to properly pinpoint pore centers and characterize the material structure. With solid understanding of the porous behavior of materials, digital recreations of media can be more precise and suitable for simulations. We introduce a complementary technique involving artificial pores to obtain improved porosity insight. Through sub-windows of an image, we can detect the likelihood of a sub-window containing a pore or an intersection of pores. For the latter classification, we bridge the gap in the pore intersection, so as to separate the pores distinctly. Finally, we demonstrate that this methodology is particularly useful for pore detection when borders are not visible.

Keywords: artificial pores, biomaterials, image analysis, pore detection.

INTRODUCTION

Polycaprolactone (PCL) foams are porous, biodegradable polymeric materials widely investigated for tissue engineering due to their biocompatibility, slow degradation rate, and low melting temperature, which confers significant malleability and allows the material to be reshaped to conform to complex geometries. This malleability, combined with a highly interconnected pore network, makes PCL foams particularly suitable for supporting cellular infiltration, where biological cells are expected to preferentially occupy larger cavities within the pore space. Accurate characterization of these cavities is therefore essential. However, pore regions that appear non-porous under imaging may in fact be connected through water-filled pathways that are poorly visible during scanning, necessitating the closure of such regions during analysis to ensure a complete and representative description of the cavity architecture. (Malikmammadov *et al.*, 2018) At its most essential description, the pore space of a material is the vacuous space not occupied by the material. Macroscopically most matter possess continuum-like behavior while their counterpart is composed of discrete empty units called pores. The pore space consists of the union of pores. For imaging purposes, the pore space is visually complementary to matter, as can be appreciated in the wide range of imaging techniques. (Blunt *et al.*, 2013) For many applications, we can learn about the material through a solid understanding of its porosity. In particular for two-dimensional images, a plethora of methods and algorithms accurately obtain the segmentation of the pore space. For binary images, a popular method is watershed, which uses the Euclidean Distance Transform (EDT) function. EDT calculates the distance away from white pixels, resulting in local maxima. In turn, these local maxima values are locations of potential pore centers. (Beucher and Meyer, 2018). Nonetheless, problems arise with pore clusters, as it sometimes fails to find each pore individually and instead considers the multiple pores as one larger entity; and viceversa, individual pores are recognized as multiple pores. (Patmonoaji *et al.*, 2020) In other instances, existing methods are unable to distinguish pore-throats from pore centers. Pore-throats are narrow slits of material as a result of pores almost intersecting as if pushing each other. To improve the segmentation accuracy of primitive watershed techniques, methods such as SNOW (Sub-Network of an Over-segmented Watershed) and other morphological tools are constantly being developed. (Gostick, 2017; Teo and Sagar, 2006; She *et al.*, 2008; Lotufo *et al.*, 2023). However, for images of our foam materials, standard methods could not distinguish merged pores as separate, especially when the borders are not visible. This motivated further pore analysis and innovative tools better suited for our needs. Hence, we complement current methods by focusing on developing techniques that find pore intersections rather than the standard strategy of going after pore centers. Our pore intersection driven approach is fundamentally different by building pore intersections artificially and then comparing with sections of the pore image; in other words, we deliberately create artificial sub-images that we know contain a pore intersection for direct comparison. In our paper, we initially lay out conditions under which a sub-image of an image can be considered a pore-throat. In the Pore-Throat Identification section we consider the quantification of white pixel distribution and density in sub-images of the main image to determine the existence of a pore-throat or pore center. In the Methodologies Using Artificial Pore Throats section we explore methodologies using construction of ”virtual pores” on high-density and low-density materials with not-visible pore boundaries. In the Results section we show results on generated images and their comparison against other classical methods. Lastly we showcase the combination of imaging methods for our foam images. We also remark the limitation that the generated images are highly idealized but serve to elucidate the utility of the artificial pore intersection methodology; and over time we expect these pore-throat based techniques to better handle different circumstances and data, especially when incorporating pore irregularity, anisotropic materials, and subpar picture quality in the form of noise stemming from imaging artifacts.

IMAGE PROCESSING TOOLS

We briefly summarize two standard image processing tools that we will be using on the images. In general, we consider an arbitrary image I with dimensions $m \times n$ for $m,n \in \mathbb{Z}_{+}$, with each entry (i,j) representing a pixel for $1 \leq i \leq m$, $1 \leq j \leq n$. The pixels in each image are indicated by values ranging from 0 to $2^d - 1$, with $d = 8$. We start with binary images having pixels being either 0 or 255. From now on, we will refer to black pixels as those having value 0 and white pixels as those having value 255.

EROSION

To remove isolated bright points, we initially parse I through repeated erosion applications. That is, given a kernel K_e with central anchor point (e.g. the pixel located at the center), we pass K_e around I and change the local central pixel in I overlapping K_e with the smallest value contained within the current overlap K_e:

$$f_e(i,j) := \min_{(i',j') \in K_e \cap I} I(i+i', j+j')$$

Thus, sufficiently isolated bright points will acquire the low values of the smaller neighboring pixels. (Chanda, 2008)

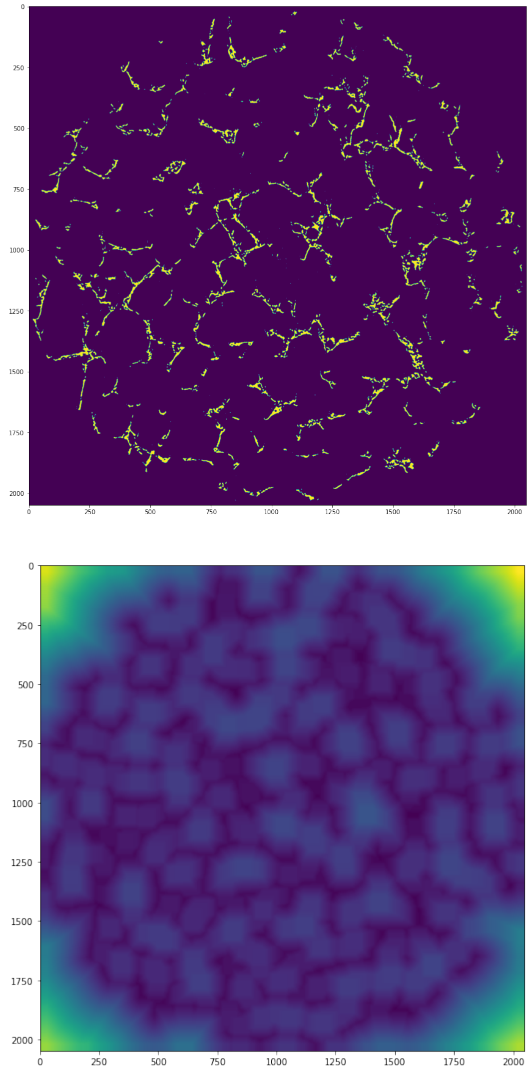

Fig. 1. *Original Image I and application of the Euclidean Distance Transform (EDT) function*

EUCLIDEAN DISTANCE TRANSFORM AND TOPOGRAPHICAL CONTOURING

To obtain locations for potential pore centers, we use the Euclidean Distance Transform (EDT). We consider the black pixels positioned the furthest away from non-black pixels. In general, porosity is represented by black pixels. We let X be the porous region of I (i.e., the black pixels of I). The Euclidean distance transform $f_{EDT} : I \to [0,\infty)$ maps each point in I to the smallest distance to the complement $I \backslash X$:

$$f_{EDT}(x) := \min\{\|x-y\| : y \in I \backslash X\}$$

Naturally for $I \backslash X$, f_{EDT} becomes zero while local non-zero maxima can be obtained in X. (Fabbri *et al.*, 2008)

PORE-THROAT IDENTIFICATION

Some areas in I will have relatively high EDT values, making them plausible prospects for pore centers as these might be local maxima. However, these are also susceptible to be zones where pores intersect, whose EDT values manifest saddle-point behavior. We seek to identify pore intersections and discard these regions as pore centers. We proceed by initially defining proper sub-images of I and then by quantifying circumstances concerning the existence of a pore-intersection.

SELECTING POTENTIAL POINTS FOR PORE CENTERS/INTERSECTIONS

We first propose an algorithm to find potential points for pore centers or intersections. We divide I into two subsets by allowing $I_b = \{p \in I : I(p) = 0\}$ to be the collection of black pixels in I and $I_w = \{p \in I : I(p) = 1\}$ to be the collection of white pixels in I. Then we consider a distance parameter $l > 0$ to create a subset $I_l \subset I$ composed of the black pixels being l away from the white pixels: $I_l = \{p \in I_b : f_{EDT}(p) > l\}$. This might still be too many pixels to be considered individually, so we introduce a closeness parameter c to discard points in I_l that are close to each other. We proceed with the following algorithm to select suitable points.

Algorithm 1: Candidate point selection

1: Initialize $l > 0$ and $c > 0$.
2: Set $I_l = \{p \in I_b : f_{\mathrm{EDT}}(p) > l\}$ and $i = 0$.
3: Let $M_i = \max_{p \in I_l} f_{\mathrm{EDT}}(p)$.
4: **while** $M_i > l$ **do**
5: Let $B_i = \{p \in I_l : f_{\mathrm{EDT}}(p) = M_i\}$.
6: Set $C_i = \{q \in I_l : \|q - p\|_2 < c \quad \forall p \in B_i\}$.
7: Increase i by 1.
8: Update $M_i = \max_{p \in I_l \setminus \bigcup_{j=0}^{i-1} C_j} f_{\mathrm{EDT}}(p)$.
9: **end while**
10: Set $B_{c,l} = \bigcup B_i$.

Here, we used $\|\cdot\|_2$ which is the standard Euclidean norm. Thus, we let $B_{c,l}$ be our starting collection of black pixels. Notice that varying the parameters c and l will result in different collections of points. Also there can be other ways of selecting points such as spacing a uniform grid. For the rest of the section, we drop the indexes c and l for notation ease.

SELECTING SUB-IMAGES OF I

Having a collection B of black pixels and before determining whether a region contains a valid pore center, we need to decide potential areas within I to explore. To that end, we state conditions for suitable sub-images of I. We observe that each black pixel in our collection $B = \{b_k\}$ is contained within a neighborhood of only black pixels, having diameter at least $2l$ because of the EDT threshold. We now seek to define square sub-windows within I for each $b \in B$. We define the distance from b to the closest white pixel by $d_{min}(b) = \min_{w \in I_w} \|b - w\|_2$. We consider an image extension parameter $\delta > 0$ to obtain a square region of interest of size $2(d+\delta) \times 2(d+\delta)$ centered at b given by $I_{b,\delta} = \{p \in I : \|b - p\|_\infty \leq d + \delta\}$. Notice that this region will include at least one white pixel.

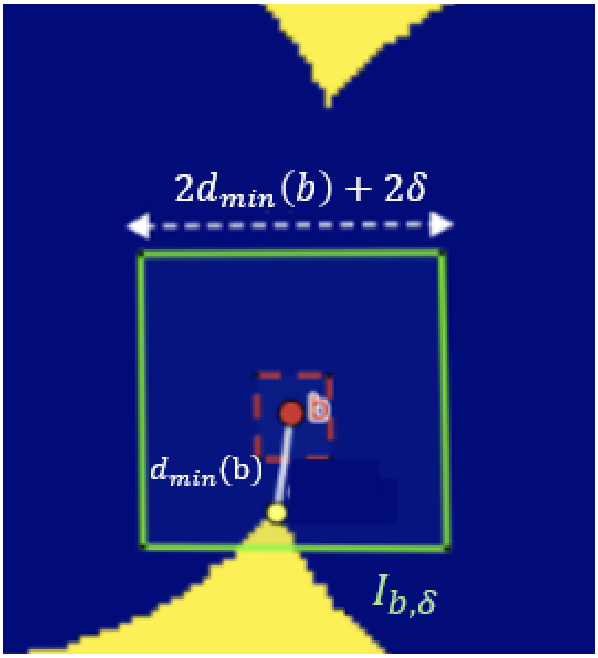

Fig. 2. *The red dashed region encompasses the black pixel neighborhood centered at the black pixel b. The distance* $d_{\min}(b)$ *is the distance from b to the closest white pixel. The sub-image* $I_{b,\delta}$ *centered at b, shown by the green box, is chosen for further pixel distribution analysis.*

Selection of thickness parameter δ

We want to obtain from $I_{b,\delta}$ information that determines the presence of a pore or pore intersection. Therefore, δ should be enough to cover some of the white pixel area as we will see in the next subsection. It is imperative that we do not overshoot the window range so as to not consider extra details not relevant to the present pore/intersection in question. So our chosen sub-image $I_{b,\delta}$ should cover enough of the region around the target to discern whether it is a pore center or intersection, but it should not be overextended to avoid processing irrelevant information. For instance, for very large sub-regions, we could actually be dealing with several complete pores instead of just one that we seek to examine individually. To impose this condition, the sub-images $I_{b,\delta}$ should not include many points in B. Fig. 3 shows how the red margins represent unsuitable areas to consider pores singly.

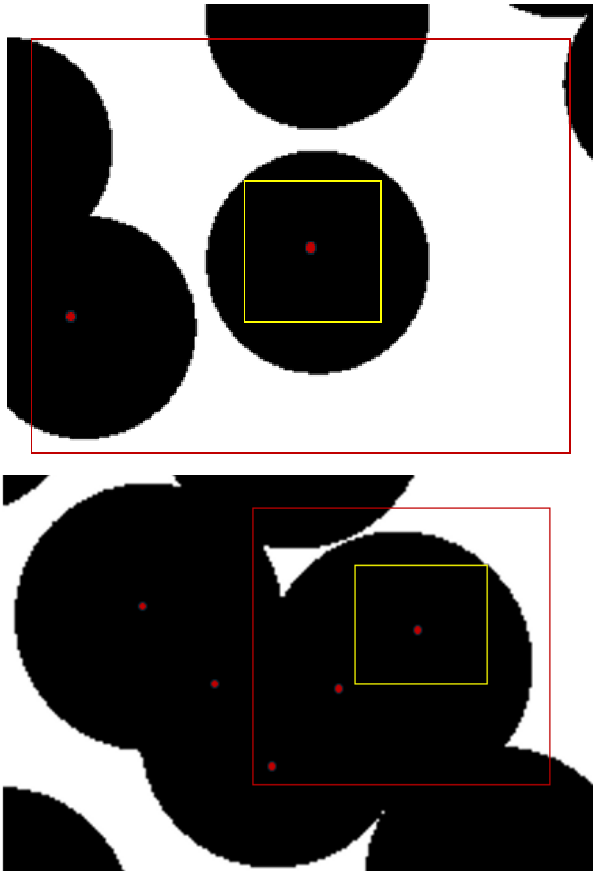

Fig. 3. *Examples of unsuitable sub-images of I. On the top, we see an isolated potential pore center (enclosed in a yellow box); but if we have a large margin, we can no longer study the pore individually. On the bottom, having too many points from B inside the red contour gives more image information than we seek to isolate.*

Thus, we suggest that the parameter δ has to be related to the density of the material. In other words, a bounding criterion for the size of δ can be proportional to $d_{min}(b)$ times the percentage of white pixels, which corresponds to the thickness of non-porous space in an isotropic material. Consequently, this restriction reduces the number of points $b \in B$ inside the sub-image. A lower bound will also be useful to include relevant white pixels in the window. We let δ be

$$(1+wp\%)d_{min}(b) \leq \delta \leq (1+2wp\%)d_{min}(b),$$

where $wp\%$ is the white pixel density in the overall image. In Fig. 4, we can observe appropriate boxes, illustrated by the green contours, for varying values of δ.

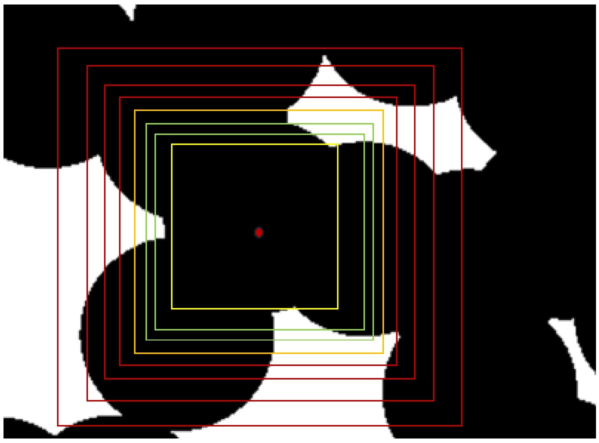

Fig. 4. *When selecting a sub-image on a target potential pore center or intersection, we expand the yellow region to choose a suitable area to investigate. The yellow contour has sides of length $2d_{\min}(b)$. The green, orange, and red margins have sides of length $2d_{\min}(b)+2\delta$; δ corresponds to values between $(1+wp\%)d_{min}(b)$ and $(1+2wp\%)d_{min}(b)$, exactly $(1+2wp\%)d_{min}(b)$, and over $(1+wp\%)d_{min}(b)$ for the green, orange, and red boxes, respectively. Anything beyond the orange lines results in overextended sub-windows containing additional irrelevant information.*

Once δ has been selected, for notation ease in the remainder of this section we shall drop the index and refer to this type of selected sub-windows by I_b. For each one of our points $b \in B$, we have a representing sub-window I_b, so we have our collection $\{I_{b_k}\}$ of sub-images. Fig. 5 shows how some sub-images I_b look in the context of the original image I.

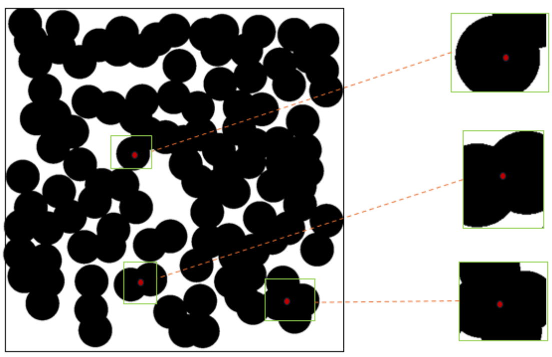

Fig. 5. *Samples of sub-images I_b in the context of the bigger picture I for potential pore center targets.*

WHITE PIXEL DISTRIBUTION QUANTIFICATION IN SUB-IMAGE

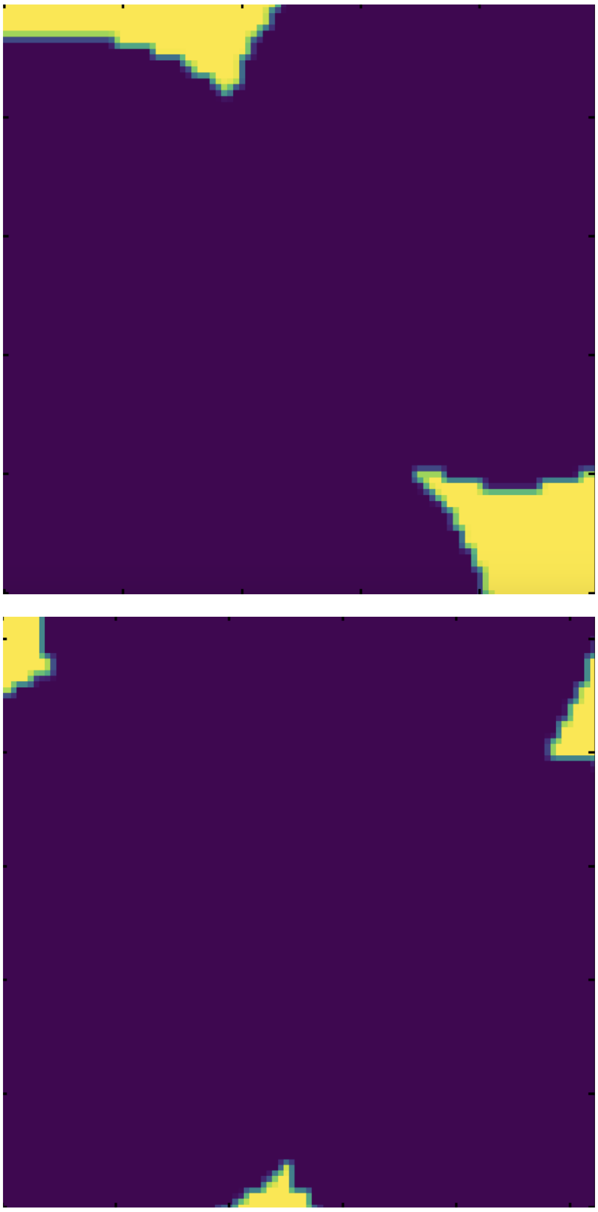

Fig. 6. *Samples of sub-images I_b containing pore intersections/throats.The top image clearly shows intersection of pores. The picture on the bottom is an intersection of three pores; given the geometrical features and sufficient isolation from the white pixels, the watershed method could interpret this as a pore center is not satisfied for large windows around the central black pixel.*

Pore Intersection

Having a sub-image $I_b \subset I$, we would now like to determine whether this window contains **exactly one** pore center or is an intersection of pores. In Fig. 6, The left image is the intersection of two pores, which the watershed method can sometimes interpret as a pore. In the same figure on the right, the center of the window is clustered by three pores; since EDT values are centrally high, it can be mistaken as containing a pore center.

We can pictorially describe this notion of the intersection of pores in Fig. 7. In a region containing a pore center, the material tends to spread out in a quasi-round manner. On the other hand, a pore intersection consists of two or more pores colliding; so when white pixels arch into the center of the sub-region, a pore-throat is most likely formed. In other words, the intersection is more likely to contain white pixels going into the center of I_b instead of having white pixels around the edges of the window, as would be apposite to a pore. This characterization is denoted as a pore throat. (Patmonoaji *et al.*, 2020) Therefore, we seek to quantify this arching of white pixels and do so by assuming the existence of pore intersections beforehand.

Artificial pore intersection construction

We want to construct a new image $I_{b,d_{int}}$ containing an artificial pore intersection and compare it with I_b with the purpose of analyzing differences or similarities. We start by obtaining a blank copy (i.e. every pixel is black) of I_b with the same dimensions and center b. Then we define a new parameter d_{int} marking the beginning of the pore intersection. This parameter has to be equal or less than $d_{\min}(b)$ in order to have a better side-by-side comparison between $I_{b,d_{int}}$ and I_b. Correspondingly, we let $\delta_{int} = (\delta + d_{\min}(b)) - d_{int}$. Without loss of generality, we will build a pore intersection in the direction from the center going down. Since b is the center of the image $I_{b,d_{int}}$, we let b_x and b_y be its coordinates in the horizontal and vertical directions, respectively. Then we change the pixel $(b_x, b_y - d_{int} - 1)$ from a black to a white pixel; that is, $I_{b,d_{int}}[b_x, b_y - d_{int} - 1] = 1$. On the next row, we turn three pixels below the previous white pixel to one, so that

$$
\begin{aligned}
I_{b,d_{int}}[b_x - 1, b_y - d_{int} - 2] &= 1 \\
I_{b,d_{int}}[b_x, b_y - d_{int} - 2] &= 1 \\
I_{b,d_{int}}[b_x + 1, b_y - d_{int} - 2] &= 1.
\end{aligned}
$$

We proceed successively by switching the pixels below it to 1 through the following iteration:

$$I_{b,d_{int}}[b_x + j, b_y - d_{int} - i] = 1$$

for $1 \leq i \leq \delta_{int}$, $-i+1 \leq j \leq i-1$. Now $I_{b,d_{int}}$ contains a pore intersection. If we wish to represent a narrower/thinner pore intersection, we can simply proceed as before but keep every row the same number s of white pixels starting from row $b_y - d_{int} - 1$):

$$I_{b,d_{int}}[b_x + j, b_y - d_{int} - i] = 1$$

for $1 \leq i \leq \delta_{int}, -s \leq j \leq s$.

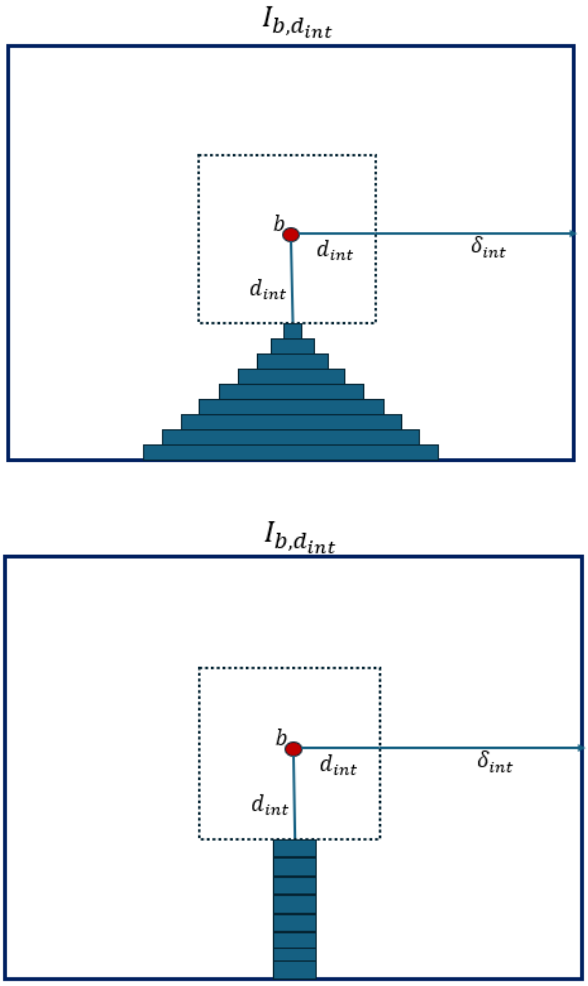

Fig. 7. ***Artificial pore intersection construction***. *At the point b in image $I_{b,d_{int}}$, we consider a distance $d_{int} \leq d_{\min}(b)$. Shown on the top side, for high density material, we can add pixels sequentially as we expand the window range in vertical and horizontal directions until reaching the edges of $I_{b,d_{int}}$. The image on the bottom depicts artificial pore construction for low-density material; this pore intersection is more narrow. Notice that to preserve the dimensions of I_b, $\delta_{int} = (\delta + d_{\min}(b)) - d_{int}$*

.

Varying the parameter d_{int} from the center until $d_{\min}(b)$ will result in representations of different pore intersections. We now introduce techniques to quantitatively compare the images I_b and $I_{b,d_{int}}$.

Quantitative comparison between I_b and $I_{b,d_{int}}$

As illustrated in the previous subsections, distinguishing the central white pixels from the ones farther out and around the edges motivates their quantification across I_b. In essence, we consider penalizing white pixels in I_b closer to the center. To this end, we define the euclidean distance function $d_b : \mathbb{R}^2 \to \mathbb{R}$ from the center b to other points: $d_b(p) := \|b - p\|_2$ for $p \in \mathbb{R}^2$. We observe that $\frac{1}{d_b(p)}$ gets smaller as p goes farther away from b. Therefore by considering a highly increasing function $f : \mathbb{R} \to \mathbb{R}$, such as the exponential function, on the range of $\frac{1}{d_b}$, we can map adjacent pixels to largely different values. For example, if we let f be the exponential function and consider the adjacent points $(b_x + x, b_y)$ and $(b_x + x + 1, b_y)$ for $x, y \in \mathbb{R}$ and $b = (b_x, b_y)$, then their respective mappings

$$\exp\left(\frac{1}{d_b(b_x + x, b_y)}\right) = \exp\left(\frac{1}{x}\right)$$

and

$$\exp\left(\frac{1}{d_b(b_x + x + 1, b_y)}\right) = \exp\left(\frac{1}{x+1}\right)$$

have very different values.

Hence, if we use these values as weights for the pixels in I_b, then positions closer to the center will reflect much higher values when this function f is applied than those farther away from the center. We now define the weight matrix $M_{I_b,f}$ for $(i, j) \in I_b$:

$$\boxed{M_{I_b,f}(i,j) := \begin{cases} f\left(\frac{1}{d_b((i,j))}\right) & (i,j) \neq (b_x, b_y) \\ f\left(\frac{1}{d_b((i,j))-1}\right) & (i,j) = (b_x, b_y). \end{cases}} \tag{1}$$

After constructing an artificial pore intersection, we use it to obtain a threshold value AP_b to compare with I_b. To accomplish this, we rely on the matrix $M_{I_b,f}$. We define $H_{I_b,true} := M_{I_b} \odot I_b$ to be the component-wise multiplication between true sub-image I_b and $M_{I_b,f}$; similarly, we let $H_{I_{b,int}} := M_{I_b,f} \odot I_{b,int}$. Observe that this is just adding weights to the white pixels with respect to their location, so that pixels closer to the center will have higher weights while the rest remains zero as before. We sum the entries of each of these matrices to obtain

$$T_b = \sum_{i,j} H_{I_b,true}(i,j), \qquad AP_b = \sum_{i,j} H_{I_{b,int}}(i,j). \tag{2}$$

T_b corresponds to the true sub-image I_b and AP_b to the artificial pore sub-image $I_{b,int}$. Finally, since the matrix $M_{I_b,f}$ penalizes centrally located pixels by making them higher valued and because AP_b is the sum of the entries of a pore intersection image, if $T_b > AP_b$, then I_b contains a pore intersection. If T_b is considerably smaller than AP_b, then it is not a pore intersection and most likely contains a pore center. New comparisons with images containing different artificial pore intersections structures can be implemented repeatedly. In this context, we notice that the function f is also a parameter assigning weights differently per function, so it is worth exploring different functions. **Remark:** Actually constructing every image $I_{b,int}$ can be expensive. Instead of building an image, we can obtain a numerical equivalence by considering integer coordinates/points away from b and summing their corresponding values of the distance weight $f\left(\frac{1}{d_b}\right)$ to get AP_b. The usage of $I_{b,int}$ in this section was mostly to illustrate how a pore intersection can be numerically evaluated, implemented, and used for comparison. We also see that for a given function f, $M_{I_b,f}$ stays the same for any sub-picture of equal dimensions. So if we have calculate a matrix large enough (e.g. at most having dimensions of I), then we calculate once and reuse it by only retaining the parts of the matrix (from the center) giving the size of I_b.

METHODOLOGIES USING ARTIFICIAL PORE THROATS

We will now introduce two methodologies for which this method of virtual pore intersection is useful. The first one is straightforward; it directly distinguishes between pore centers and intersections. It uses an additional parameter: the number of white pixels contained within the sub-image I_b (i.e. amount of white pixel area). It is mostly suitable to images having high white pixel density. We will be referring to images having over 10% of white pixels as high white pixel density, or high density for short; otherwise they will be considered as having low white pixel density, or low density. The second method identifies pore intersections and stitches the ends of the intersections so as to close out the pores. Then having more closed pores, this approach can be combined with other existing techniques to find pores centers directly. There is increased ambiguity between pore centers and intersections with fewer pixels present, so the second methodology is more practical for low-density images. We refer to Table 1 for a list of relevant parameters by methodology and their intended purpose.

METHODOLOGY 1: USING AREA IN SUB-IMAGE I_b

We proceed as laid out in the previous to obtain our set of potential pore centers/intersections B and selected sub-images I_b, for given values of parameters l, c, δ, f. We then calculate the values T_b and AP_b. We make the observation that for areas with high density, there are more white pixels around the pore than in the narrow pore-throat for similar window size. An example of this can be observed in Fig. 8. This motivates using the number of white pixels present as an additional determining factor $A_{wp}(I_b)$ when determining a pore center. We define a parametric threshold $A_{wp,cutoff}$ that varies by image I. Then if $AP_b > T_b$ and the number of white pixels present in I_b is high(i.e. greater than $A_{wp,cutoff}$, then we determine that I_b contains a pore center.

Fig. 8. *We have sub-images of a pore and a pore intersection on the top and bottom pictures, respectively. The white pixel density of the top side is much higher than the white pixel density of a pore intersection, motivating the parametrization of pixel density.*

METHODOLOGY 2: STITCHING ENDS OF INTERSECTIONS

For this method, we use the information from EDT to see how intersections behave for places when white pixel density is low. When we locate an intersection, we put the ends of the intersection together to close out some of the pores. We convert the porous space into high white pixel density area by reversing the roles. Then eroding this porous material, which is now white pixels, we use criteria and observations previously obtained to fuse ends of pore intersections.

Mask split definition

For materials with lower white pixel density, it can be harder to determine from area alone whether a sub-image I_b contains a pore center or is a pore intersection, particularly when the pore boundaries are not clearly visible. We first consider the behavior of eroding masks created from EDT thresholds. We define a lower EDT threshold β (e.g. $\beta = 15$), similar to what we did in the previous section with parameter l. Then, we create a pore mask image $I_{mask}(\beta)$ of I with white pixels only where $f_{EDT}(I) \geq \beta$:

$$I_{mask}(\beta)[i,j] := \begin{cases} 1 & \text{if } f_{EDT}(I[i,j]) \geq \beta \\ 0 & \text{otherwise.} \end{cases}$$

In Fig. 9, an example of this $I_{mask}(\beta = 15)$ is portrayed by the dense white pixel mask region, which in this case are all the pixels located at least $\beta = 15$ away from the matter (non-zero) pixels in the original image. As can be seen on the left side of Fig. 9, in regions with pore intersections, the masks (in yellow) tend to be narrower than in areas with pores. These bottlenecks result from only two material pixels in opposite sides pushing the masks in. In fact, the hollowing of the mask tends to increase as more material pixels are present and distributed around. Hence, if we erode $I_{mask}(\beta)$, the narrow areas will be chiseled away and split up into two smaller chunks with sharp ends. This is shown in Fig. 9. However, as depicted on the right image of Fig. 10, we need **exactly two** sharp ends on approximately opposite sides to consider a full intersection, not just one sharp end. This motivates the discovery of an additional characteristic to detect regions when the mask branches separates from other areas. We will be referring to these areas as **mask splits**. These mask splits locally look like pore intersections of the kind seen in Fig. 6. We use equations 1 and 2 to determine the existence of a mask split, hence a potential pore intersection. We recall that given two sets A and K, the process of erosion is defined as translating a set A by all points in the set K and then taking the intersection: $A \ominus K = \cap\{A_z : z \in K\}$, where $A_z = \{a+z : a \in A\}$. Chen and Haralick (1995)

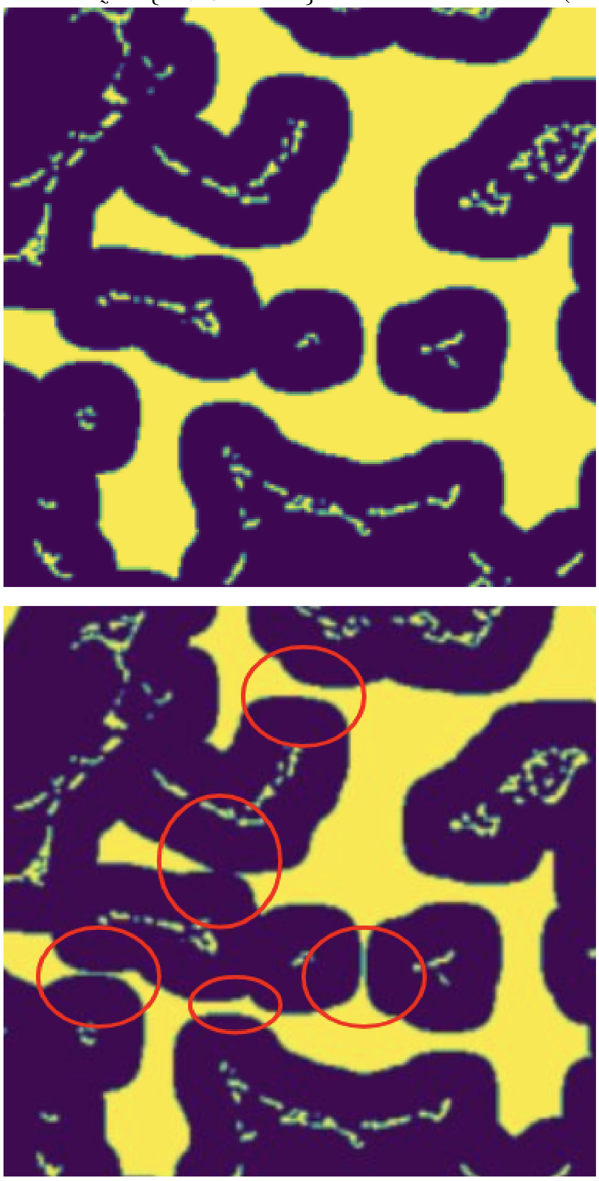

Fig. 9. *On the top image, we have binary masks for EDT values above 15. Whenever there is a pore intersection, the connecting areas of the mask tend to shrink. On the bottom picture, erosion results in shrinking these bottlenecks, making it easier to detect pore intersections.*

Determining set of points of masks splits

We set a window size lower bound $s_{\min}$ and consider the parameter $s \geq s_{\min}$. Then to find these potential splits, we search for black pixel-only windows of size s by s within the union of I and $I_{mask}(\beta)$. We let B_{mask} be the centers of these black pixel-only neighborhoods. We notice that while the foam image I itself is not a high white pixel density material, the mask image $I_{mask}(\beta)$ of the porous region is. As a result, some of the sharp ends have similar behavior to the high-density material considered in the previous subsection 4.1. This implies that using the technique laid out in subsection 3.3.2 we can find sub-images $I_{b,mask}$ from the larger I_{mask} containing sharp ends mimicking pore intersections of high-density materials.

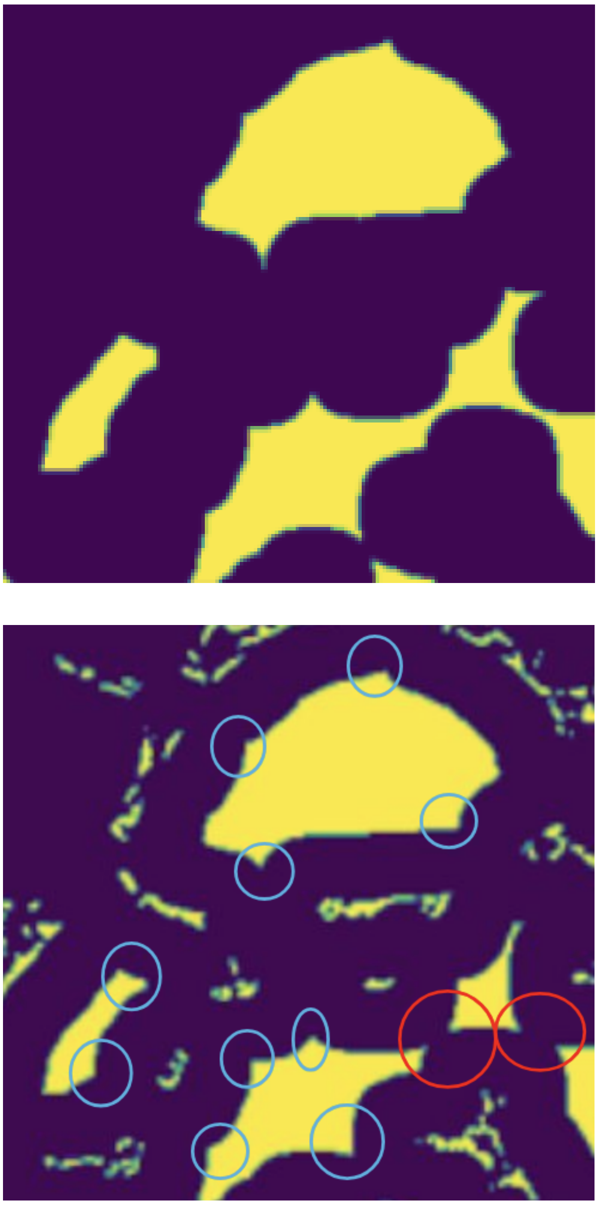

Fig. 10. *The region on the top shows a less eroded mask (in yellow) than the picture on the bottom; we can observe, how the area transforms according to EDT cutfoff. There are places where the mask potentially splits into different components and has sharper ends; we call these mask splits. The red circles in the bottom correspond to proper mask splits (i.e. where* ***two*** *ends of white pixel regions almost touch) while the blue circles pinpoint regions with* ***only one*** *sharp end present in the neighborhood, mimicking pore intersections of a high density material.*

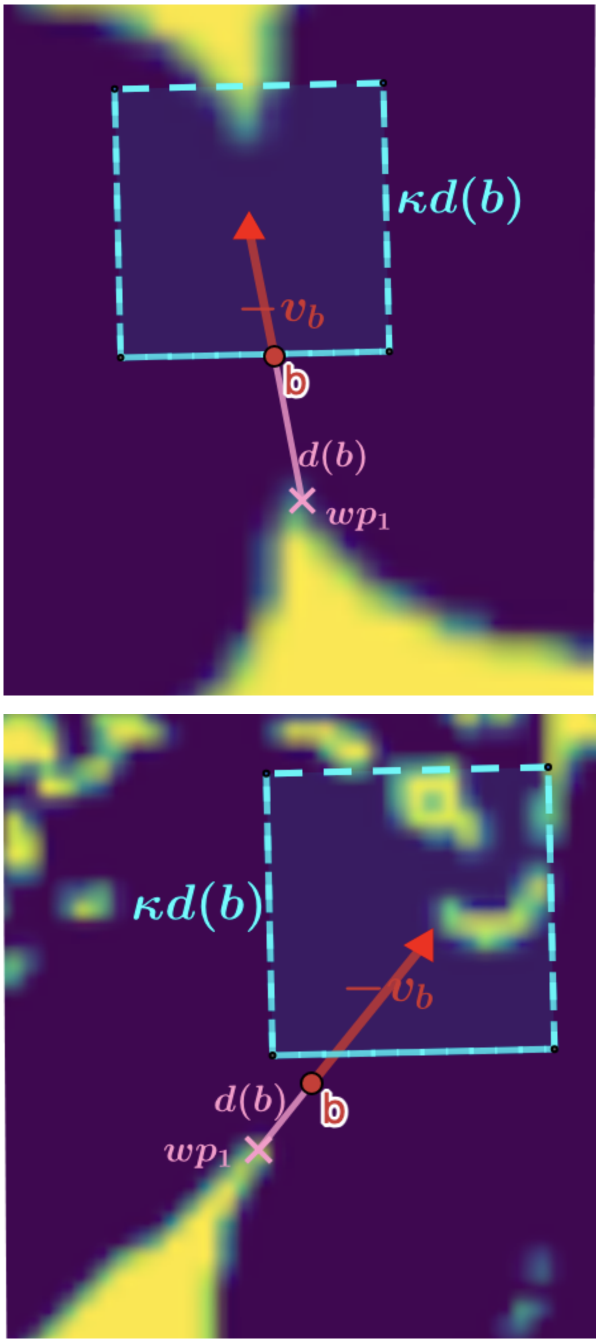

Fig. 11. *Mask splits can be located by finding the closest white pixel from a black pixel b. A box can be calculated in the other direction to find white pixels. On the top, a successful mask split can be found, while on the bottom, there are no white pixels from the mask image I_{mask}. The white pixels in the blue box of the bottom image belong to I and not to I_{mask}.*

Drawing boxes from masks splits to find intersections and stitch their ends

We then declare a value $\kappa > 0$ to be a scalar that we will use in the next operations. For each $b \in B_{mask}$, we find the closest white pixel wp_1 and its distance $d(b)$ to it. Then we calculate the vector v_b from b to wp_1, and consider the vector $-v_b$ in the opposite direction. We let the other endpoint of $-v_b$ be the center of a box of side $\kappa d(b)$. If this box intersects white pixels in $I_{b,mask}$, then we conclude that this is an intersection. This is shown in Fig. 11. Notice that κ is bounded by $2\sqrt{2}$; otherwise, the box will intersect wp_1. When we determine that b is in a region of a mask split, we look for the closest two white pixels from b to I in relatively opposite directions, similar to how it was just done with I_{mask}. Then we draw a line between these two points to stitch up the intersection and close the pore boundary more. The left portion of Fig. 12 depicts lines between mask splits.

Using erosion to find pore centers with updated stitches

After several iterations of erosion, the pore boundaries are better connected, enhancing the use of watershed techniques and morphological tools. We let $\alpha := \max_{x \in I} f_{EDT}(x)$ be the largest EDT value in I and $t_{\max}$ the maximum number of erosions we wish to set. We let X_k be connected subsets of the mask image $I_{mask,t}$ after $t \leq t_{\max}$ erosions on I. For each connected subset X_k, we calculate the area $\|X_k\|$ and centroid C_{X_k}, and we set

$$\varepsilon_k := \sqrt{\frac{\|X_k\|}{\pi}} + \delta_t,$$

where δ_t is the window parameter when expanding from b to form the sub-images I_b. If $\alpha < \varepsilon_k$, then ε_k corresponds to a ball that is larger than the biggest possible pore in I. Therefore, we only consider $\varepsilon_k \geq \alpha$. We seek to compare the region X_k to the ball $B(C_{X_k}, \varepsilon_k)$ centered at C_{X_k} with radius ε. We now define an image I_{X_k} with all zero values except where X_k is nonzero in $I_{mask,t}$; similarly, we let $I_{B(C_{X_k}, \varepsilon_k)}$ be filled with all zero values except for $B(C_{X_k}, \varepsilon_k)$.

We calculate the intersection of these two images, and if it is not empty, then X_k is not contained within a large ball. This implies that the region X_k is distributed and consists of connected pores. If $I_{X_k} \cap I_{B(C_{X_k})} \neq \emptyset$, then X_k corresponds to a pore with pore center C_{X_k}. This difference is illustrated in Fig. 13. We then update I by allowing it to become $I \cup I_{X_k}$, patching up the pore X_k.

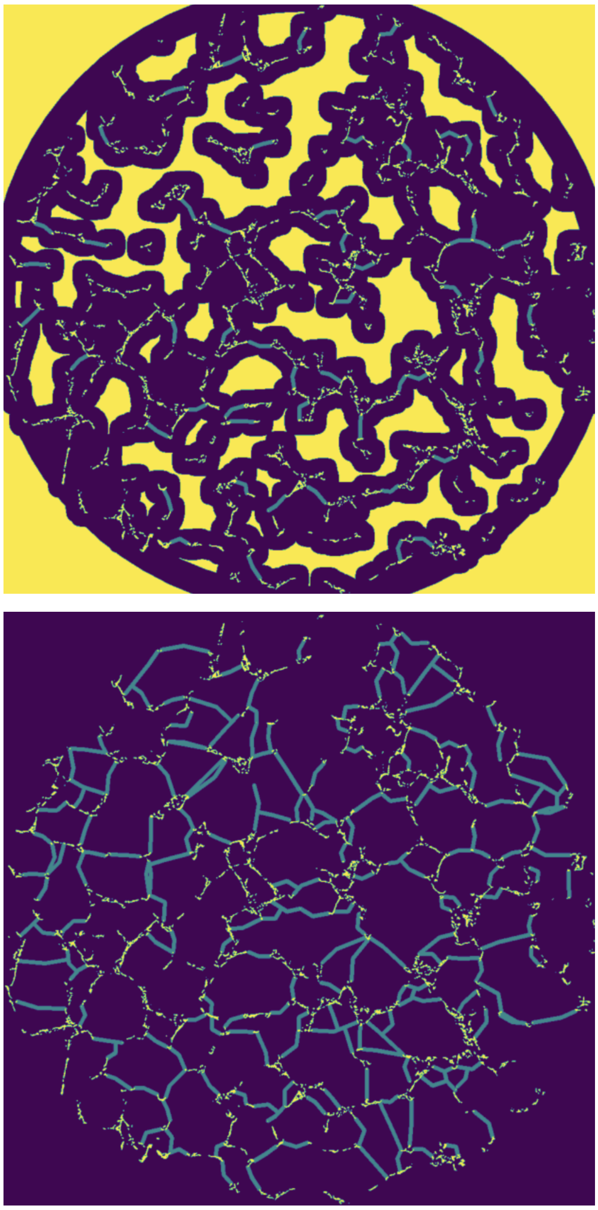

Fig. 12. *On the top, the not-visible boundaries of the pores are stitched up at the intersection points after several iterations. The bottom image shows more closed off pores after several iterations.*

We recalculate EDT values on I and repeat the process until we have exhausted the number of iterations and window size for black pixel boxes (i.e. we can no longer find a black pixel- only neighborhood for $s > s_{\min}$).

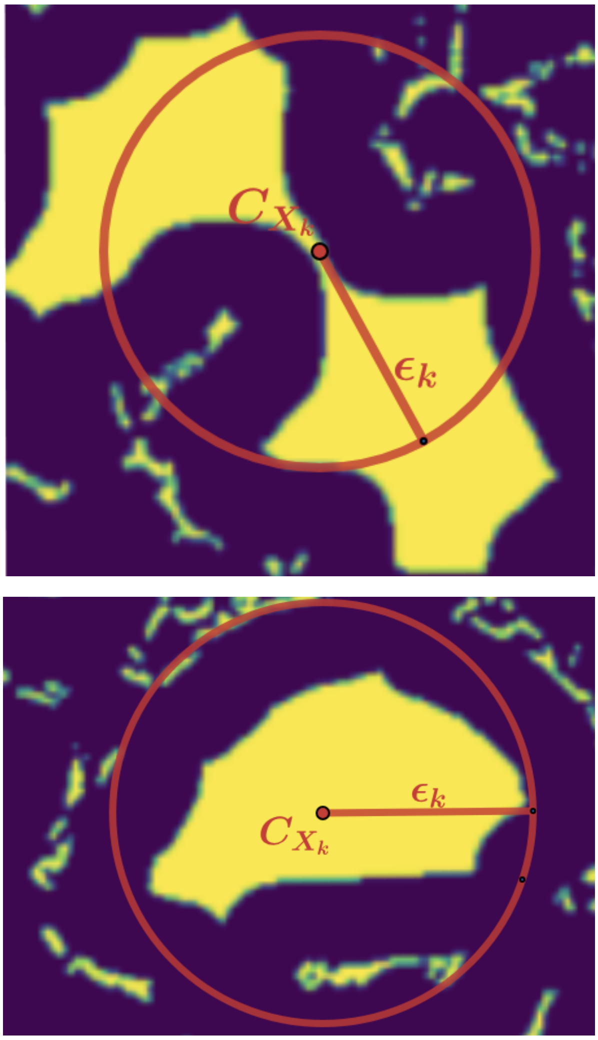

Fig. 13. *On the top, the connected region is not enclosed within a ball of corresponding radius. The bottom image shows a pore through containment within a ball.*

RESULTS

SIMULATION STUDY - GENERATED PORES

We explored computationally the aforementioned criteria and methodology on images containing artificial pores of radius of 50 pixels and compared our results against the standard watershed algorithm. For each pore radius, we generated random points in a plane and expanded circles around these. We obtained twenty images for each set and calculated the average for each performance benchmark. In particular, we calculated how far away from the true centers were the estimates for each method in terms of pixel distance. To avoid instances of double counting, every time a suitable pore center was found, the image was patched with a circle to avoid looking again in the area. For our method, we had parameter intervals over which we ran the computations.

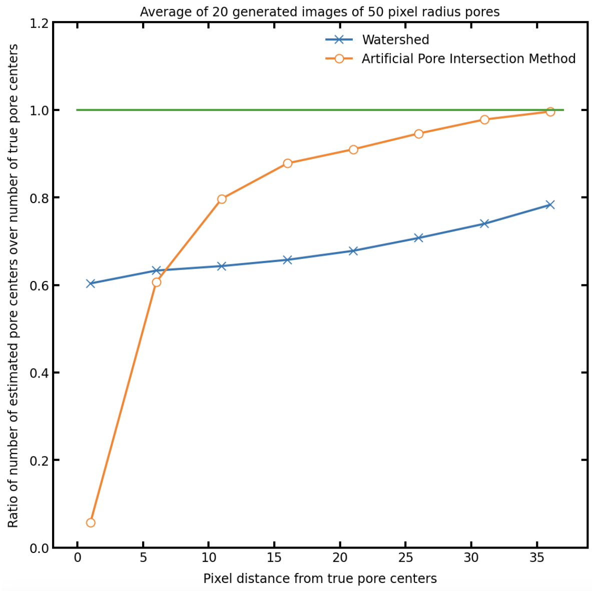

Fig. 14. *The artificial pore intersection and watershed methods are compared in terms of how far away the coordinates are from the true data for pores of radius of 50 pixels.*

Fig. 14 shows that our method is able to find more coordinates close to the true pore centers; in fact it manages to find pore centers below a distance of ten pixels, with over 80% matches. However, we can also see that as the pixel distance is increased, the number of points also goes up for all methods; this is most likely due to some coordinates lying in intersections of these pores rather than closer to the true centers. In other words, at times our method approximates two pores instead of one, so that the true count is fractionally and slightly higher than it is supposed to be for higher pixel distance away from pore centers; to thwart this we tried to remove neighboring points in circles of the corresponding pore radius. Note also that, as seen in Fig. 15, our frame based criteria finds clustered pores more accurately, especially as these are ambiguous to tell apart from a bigger pore. In fact, our methodology discerns more reliably whenever there are pore throats, while watershed fails to recognize some obvious pore intersections and mistakenly classifies them as pore centers. Fig. 16 shows a full comparison of the estimated pore centers using our method and watershed.

All the graphs show that watershed has initially a higher slope than our method. This is mainly due to watershed achieving more centralized estimates, as we relied on the initial potential points B scattered around the image. Moreover, although our estimated pores are

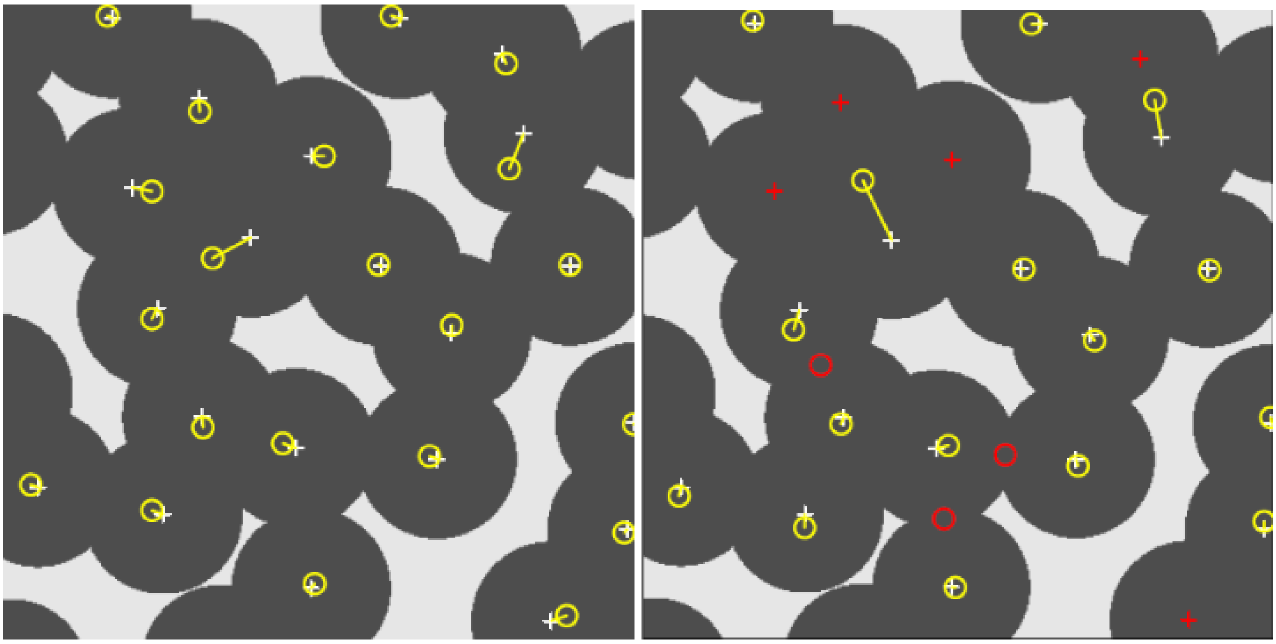

Fig. 15. *When pores are clustered, our pore criteria is able to distinguish most of these pores apart (left) while the watershed algorithm fails to recognize these bundles as collection of pores (right). White crosses indicate true pore centers, yellow circles correspond to estimates close to true data, and and the red circles/crosses are missed targets.*

Table 1. ***Parameter summary for both methodologies***

White pixel area	Intersection Stitching	Reason
l: distance away from white pixels for EDT threshold	$s_{\min}$: lower bound for length of black pixel-only window side	Pore intersection candidate locations
c : separation of points in B		Minimum spacing among candidate point locations
δ: added window space	δ_t: added window space for iteration t	Additional padding to determine pore intersection material in the margins of the box
f: increasing function	f: increasing function	Strength of values within box (How larger are values closer to center of box than away from it)
$M_{I_b,f}$: Artificial pore intersection matrix	$M_{I_{b,mask},f}$: Artificial pore intersection matrix	Numerical values of box by distance to center and function f
$A_{wp,cutoff}$: white pixel area threshold		White pixel quantity consideration (density)
	β: Lower EDT threshold	White pixel quantity of non-porous region complement for mask shrinkage examination (i.e. how far into the pore is it desirable to obtain a complement mask)
	κ: Mask split box scalar	Size of box for finding whether other white pixels in mask I_{mask} exist besides wp_1
	$t_{\max}$: maximum number of erosion iterations	Number of times the pore mask is shrank to determine pore intersection spikes.

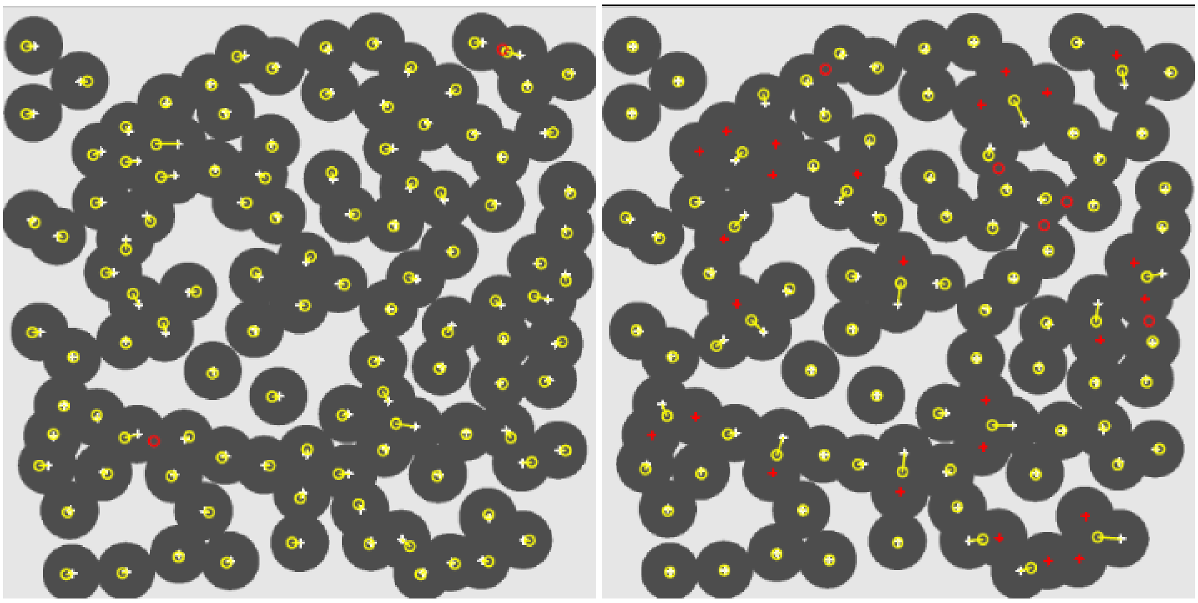

Fig. 16. *Pore center estimates of radius 50 pixels after using our pore intersection method (left) vs watershed (right). White crosses indicate true pore centers, yellow circles correspond to estimates close to true data, and and the red circles/crosses are missed targets.*

decentralized, this can be corrected by looking at the direction of the nearest pixel and pushing away by a few pixels the predicted center in the direction of the vector formed from the nearest pixel and the estimated center.

Next, to consider other metrics, we generated new sets of images by forming circles with the respective radii and the coordinates obtained from each method. Fig. 18 shows the images of pores of radius 50 pixels with the estimated pore centers.

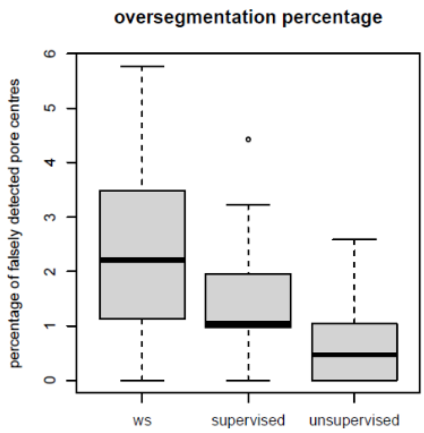

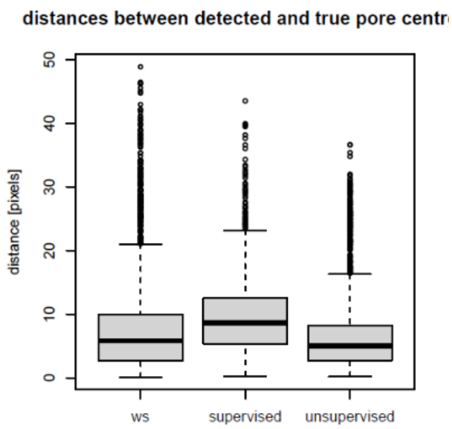

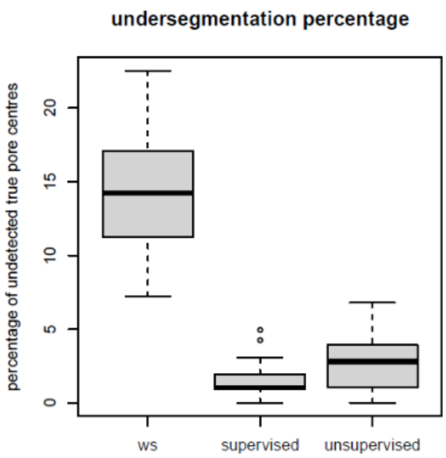

Fig. 17. *Statistical summary of undersegmentation (bottom-left), oversegmentation (top), and distance from center (bottom-right).*

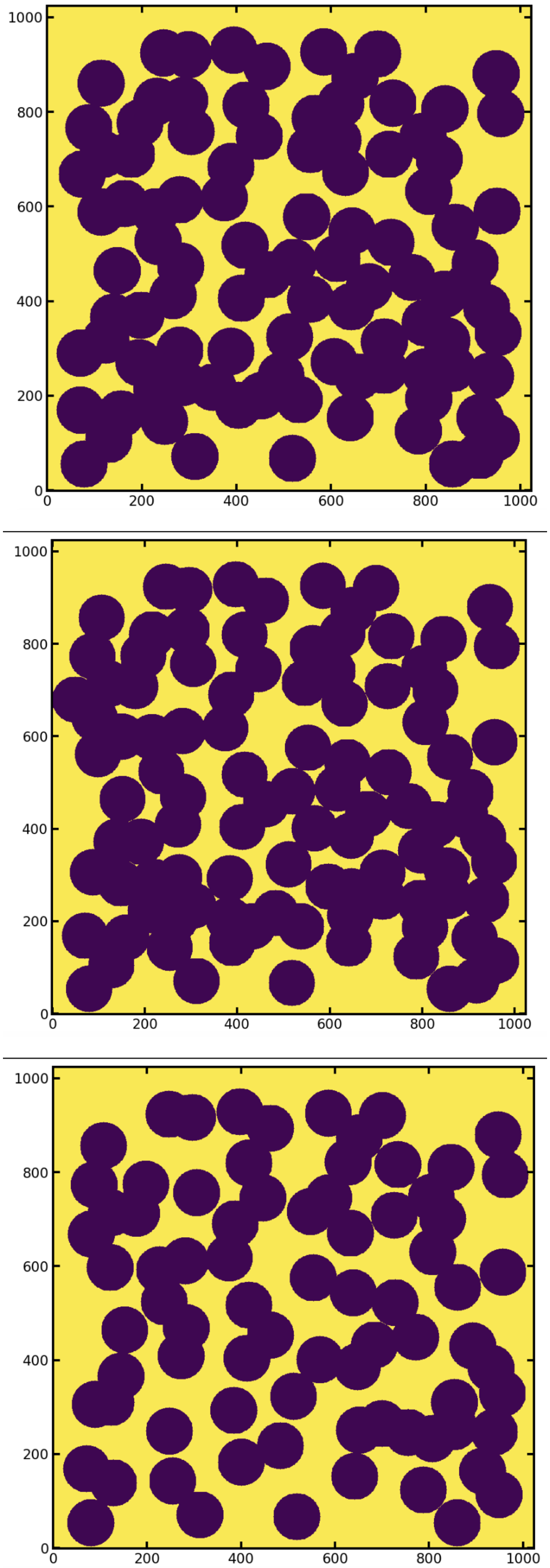

Fig. 18. *Generated pores using estimated data. The true pore image is on the left, the image generated using the artificial pore intersection method is on the center, and the watershed image is on the right.*

Then we can compare the newly formed images with the original artificial images. We briefly summarize the metrics used for comparison between two images I_1 and I_2.

- **Hamming Distance:** Counts the number of pixels that differ in both images. Lower values indicate fewer mismatches. Zhang *et al.* (2021)
- **Jaccard Index (IoU):** Also known as the intersection over union, it measures the similarity between both images using the formula
$$\frac{|I_1 \cap I_2|}{|I_1 \cup I_2|},$$
ranging between 0 and 1 with a value closer to 1 indicating that the images are closer to each other. Costa (2021)
- **Dice Coefficient:** This metric is akin to Jaccard index with an emphasis on intersection when assessing overlap. It uses the expression
$$\frac{2|I_1 \cap I_2}{|I_1| + |I_2|}.$$
Like the previous metric, a higher value is more desirable.Guindon and Zhang (2017)
- **Accuracy:** It evaluates the proportion of correct pixels by considering the true negatives and true positives in the following relation
$$\frac{TP + TN}{TP + TN + FP + FN},$$
where TP is the number of correctly classified white pixels, TN the number of correctly classified black pixels, FP the number of incorrectly labeling black pixels as white pixels, and FN is the misclassification of white pixels as black pixels. Higher values indicate better prediction.Eder *et al.* (2013)
- **Hausdorff Distance:** It evaluates the greatest of all distances from a point in one image to the closest point in the other images. It is presented by
$$H(I_1, I_2) = \max(h(I_1, I_2), h(I_2, I_1)),$$
where $h(I_1, I_2) = \max_{u \in I_1} \min_{v \in I_2} \|u - v\|$ and $\|\cdot\|$ is a norm such as the L_2 (Euclidean norm). Lower values mean that boundaries are better shaped to the true boundaries.Huttenlocher *et al.* (1993)

As can be seen from Table 2, the artificial pore intersection method is slightly superior than watershed in all the metrics (i.e. lower Hamming Distance, higher Jaccard index, higher dice coefficient, higher accuracy, and lower Hausdorff). We computed our results in a Macbook air M1-chip machine with 8-core CPU and 7-core GPU. For the images of pores with radius 25, 50, and 100, the watershed

Table 2. *Average of estimated generated pores with 50 pixel radius*

Method	Hamming Distance	Jaccard Index	Dice Coefficient	Accuracy	Hausdorff
Artificial Pore Intersection	2852.1	0.0435	1.82×10^{-4}	0.0289	155.11
Watershed	5498.3	0.0393	1.73×10^{-4}	0.0254	244.91

was significantly faster clocking at 2.2 seconds, 2.3 seconds, and 2.6 seconds, respectively, compared to our method recording 91 seconds, 32.8 seconds, and 2.5 seconds, respectively. This discrepancy is mainly due to the use of well-known library packages for watershed methods.Gostick *et al.* (2019) Also, some of the parameters such as the artificial pore construction and using different intersections a priori require more iterations to enable more precision. And different parameters such as overall area, thickness around box after finding initial pixel, and function to penalize inner pixels were considered in implementing the process.

POLYCAPROLACTONE (PCL) CREATION AND IMAGE GENERATION

To begin the scaffold fabrication process, various sample formulations were prepared by adjusting the concentrations of polycaprolactone (PCL) and water. This ternary mixture consisted of PCL as the polymer, 1,4-dioxane as the solvent, and water as the non-solvent, with freezing points of -62°C, 11.9°C, and 0°C, respectively. Mixtures were stirred and gently heated until fully homogeneous. Solutions were carefully pipetted into slender polymethyl methacrylate (PMMA) tubes, each approximately 22 mm in height and 3 mm in diameter. The base of each tube was sealed with parafilm to prevent leakage, ensuring a secure environment for the mixture. The filled tubes were placed on dry ice for rapid freezing. As the mixtures solidified, they naturally contracted, so additional solution was added to fill any gaps, preventing the formation of air pockets or empty spaces—an important consideration since the tube dimensions were specifically selected for subsequent imaging analyses. Once fully frozen, samples were transferred to a freeze-dryer (Alpha 2-4 LSCbasic) and subjected to lyophilization for 48 hours at approximately 0.1 mbar and -39°C. This process removed the polymer-lean phase, leaving behind only the polymer-rich porous scaffold. After freeze-drying, the samples were stored in a refrigerator to preserve their structure until further analysis. For structural characterization, the scaffolds were transported to the European Synchrotron Radiation Facility (ESRF), where synchrotron x-ray tomography was employed. Imaging was conducted at a resolution of 2048×2048 pixels, offering a spatial resolution of 3.45 pixels per micrometer and an effective pixel size of 0.290 micrometers per pixel. The image generation steps were carried out using Simpleware ScanIP V-2024.06.Synopsys, Inc. (2024) A couple of samples are shown in Fig. 19.

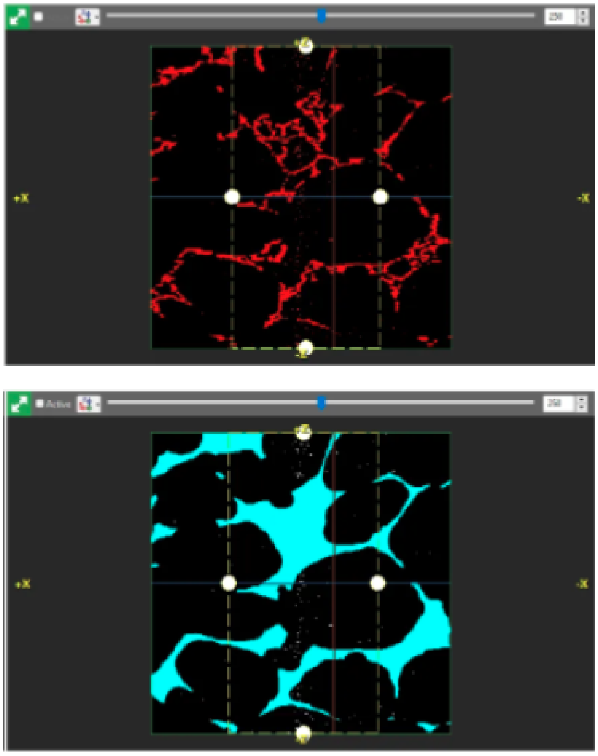

Fig. 19. *PCL images from tomography were generated and preprocessed using Simpleware ScanIP V-2024.06*

PCL RESULTS

The motivation behind the development of our pore-throat scheme was to better recognize unseen pore intersections, present in the form of water, from equally separated pore centers. For our purposes, these pore-throats are represented by black pixels with relatively high EDT values. For substantially large EDT values, watershed is reliable; but for smaller pores, it does not always distinguish properly an intersection from a pore center. On the other hand, as exemplified in Fig. 20, whenever the mask was sufficiently isolated and contained fully within a circle of comparable area, as explained in the previous section, we kept the mask and patched to the newly found white pixels to omit looking for candidates in those regions.

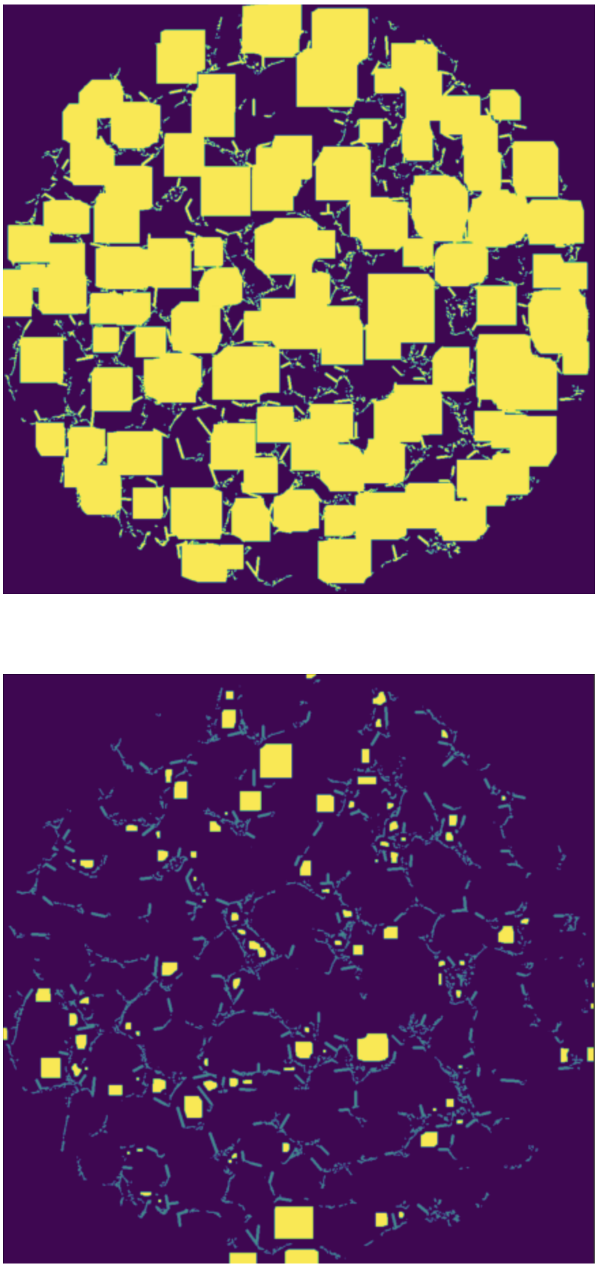

Fig. 20. *Both images show patching of large (top) and small (bottom) pores after finding masks that most likely represent pores to steer clear of those regions.*

Lastly, Fig. 21 displays the final result of our implementation of the artificial pore-intersection algorithm versus watershed. In general, our method is more careful than watershed in not mislabeling pore throats as pores. For bigger pores, either method is reliable; but delicate threading and parametrization is required to find suitable estimates for smaller pores. The pore-throat based method took 37 seconds to implement while it took 6.7 seconds using watershed.

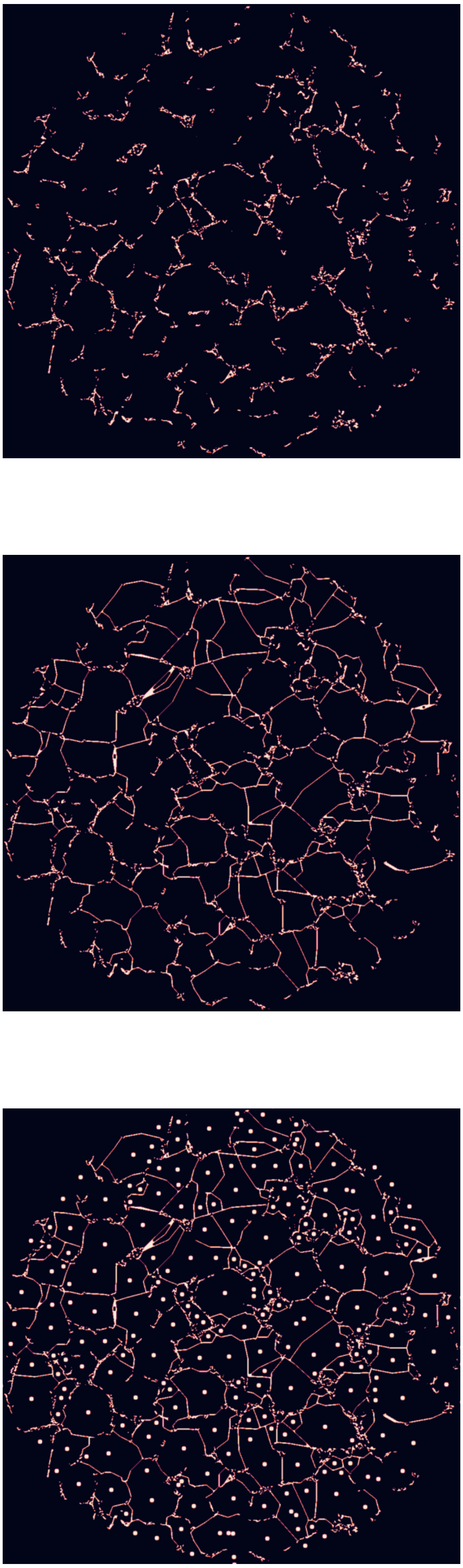

Fig. 21. *Using the second methodology, we can close out some pores and find the centers.*

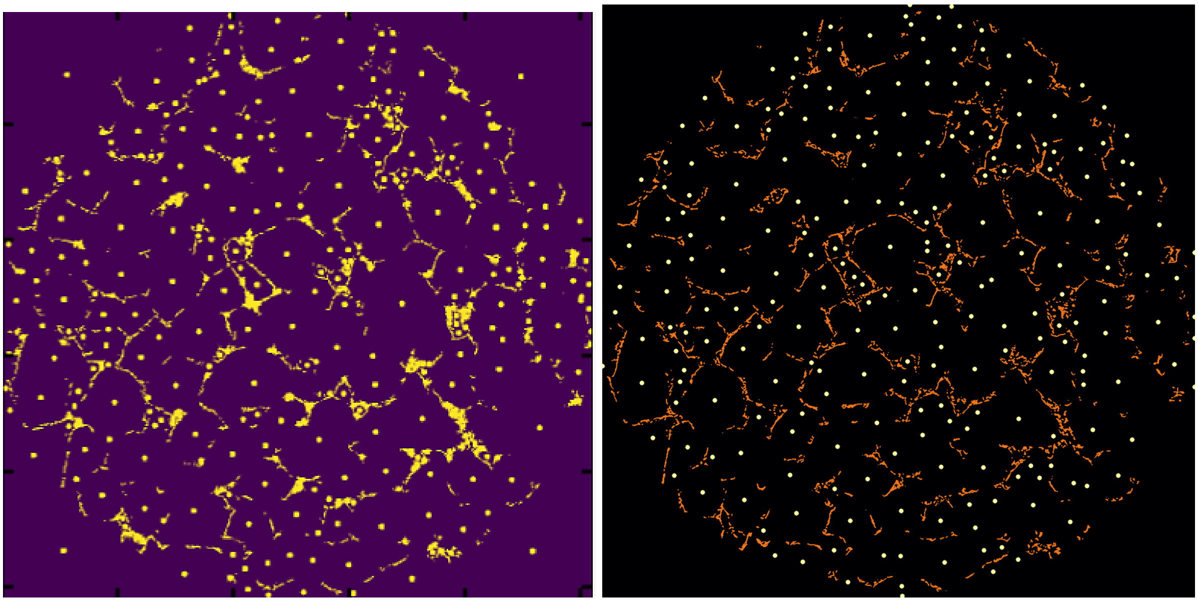

Fig. 22. *Foam image for pore estimation using watershed (left) and our methodology (right)*

CONCLUSION

We believe our method is strong enough to estimate pores in regions where watershed fails, whether it is a cluster or pore intersections. However, this is achieved at the expense of increased time complexity and semi-automatic implementation. Nonetheless, the noticeable increase in accuracy is worth the tradeoff. This is particularly necessary as we attempt to explore certain notions of structures that might otherwise be missing or poorly understood as a consequence of insufficient approximation. In the case of complex porous structures, such as when pore divisions are not clear, it could be useful to draw missing boundaries to better understand the material distribution. While some pore center estimates seem jumbled in our method, they help shape the structure much truer to their geometry. In general, the construction of artificial pore intersections to detect pore intersections and estimate pore centers is reliable but could be improved for more general cases.

DATA AVAILABILITY STATEMENT

Controlled access: Access to data is restricted due to sensitive experimental parameters and to being part of ongoing institutional research. Qualified researchers may request access for validation purposes by contacting Dr. Jens Vinge Nygaard via institutional email.

ACKNOWLEDGMENTS

We are very greatful to the Villum foundation, who funded this research, including the salaries of I. Martinez and C. Suarez Londoño, with grant no. 50104.

REFERENCES

Beucher S, Meyer F (2018). The morphological approach to segmentation: the watershed transformation. In: Mathematical morphology in image processing. CRC Press, pp. 433–81.

Blunt MJ, Bijeljic B, Dong H, Gharbi O, Iglauer S, Mostaghimi P, Paluszny A, Pentland C (2013). Pore-Scale Imaging and Modelling. Adv Water Resour 51:197–216.

Chanda B (2008). Morphological algorithms for image processing. IETE Tech Rev 25:9–18.

Chen S, Haralick RM (1995). Recursive erosion, dilation, opening, and closing transforms. IEEE Trans Image Process 4:335–45.

Costa LF (2021). Further generalizations of the Jaccard index. arXiv preprint arXiv:2110.09619.

Eder M, Brockmann G, Zimmermann A, Papadopoulos MA, Schwenzer-Zimmerer K, Zeilhofer HF, Sader R, Papadopulos NA, Kovacs L (2013). Evaluation of precision and accuracy assessment of different 3-D surface imaging systems for biomedical purposes. J Digit Imaging 26:163–72.

Fabbri R, Costa LF, Torelli JC, Bruno OM (2008). 2D Euclidean Distance Transform Algorithms: A

Comparative Survey. ACM Comput Surv 40:2:1–2:44.

Gostick J, Khan ZA, Tranter TG, Kok MDR, Agnaou M, Sadeghi MA, Jervis R (2019). PoreSpy: A Python Toolkit for Quantitative Analysis of Porous Media Images. J Open Source Softw.

Gostick JT (2017). Versatile and efficient pore network extraction method using marker-based watershed segmentation. Phys Rev E 96:023307.

Goyal M (2011). Morphological image processing. IJCST 2:59.

Guindon B, Zhang Y (2017). Application of the dice coefficient to accuracy assessment of object-based image classification. Can J Remote Sens 43:48–61.

Huttenlocher DP, Klanderman GA, Rucklidge WJ (1993). Comparing images using the Hausdorff distance. IEEE Trans Pattern Anal Mach Intell 15:850–63.

Jung A, Redenbach C, Schladitz K, Staub S (2022). 3D Image-Based Stochastic Micro-structure Modelling of Foams for Simulating Elasticity. In: Research in Mathematics of Materials Science. Springer, pp. 257–81.

Kornilov A, Safonov I, Yakimchuk I (2022). A review of watershed implementations for segmentation of volumetric images. J Imaging 8:127.

Leblanc C, Kilingar NG, Jung A, Kamel KEM, Massart TJ, Noels L, Béchet E (2022). Analysis of an open foam generated from computerized tomography scans of physical foam samples. Int J Numer Meth Eng 123:4267–95.

Lindeberg T (1993). Discrete derivative approximations with scale-space properties: A basis for low-level feature extraction. J Math Imaging Vis 3:349–76.

Lotufo RA, Audigier R, Saude AV, Machado RC (2023). Morphological image processing. In: Microscope image processing. Elsevier, pp. 75–117.

Macia I (2007). Generalized computation of Gaussian derivatives using itk. Insight J 1–14.

Malikmammadov E, Tanir TE, Kiziltay A, Hasirci V, Hasirci N (2018). PCL and PCL-based Materials in Biomedical Applications. J Biomater Sci Polym Ed 29:863–93.

Moreaud M, Chaniot J, Fournel T, Becker JM, Sorbier L (2018). Multi-scale stochastic morphological models for 3D complex microstructures. In: 2018 17th Workshop on Information Optics (WIO). IEEE, pp. 1–3.

Nimmo JR (2004). Porosity and pore size distribution. Encyclopedia of Soils in the Environment 3:295–303.

Patmonoaji A, Tsuji K, Suekane T (2020). Pore-throat characterization of unconsolidated porous media using watershed-segmentation algorithm. Powder Technol 362:635–644.

Raid AM, Khedr WM, El-Dosuky MA, Aoud M (2014). Image restoration based on morphological operations. Int J Comput Sci Eng Inf Technol 4:9–21.

Re GL, Lopresti F, Petrucci G, Scaffaro R (2015). A facile method to determine pore size distribution in porous scaffold by using image processing. Micron 76:37–45.

Redenbach C, Schladitz K, Vecchio I, Wirjadi O (2014). Image analysis for microstructures based on stochastic models. GAMM-Mitt 37:281–305.

Safonov IV, Mavrin GN, Kryzhanovsky KA (2006). Segmentation of convex cells with partially undefined boundaries. Pattern Recognit Image Anal 16:46–9.

Safonov IV, Mavrin GN, Kryzhanovsky KA (2008). Segmentation of convex cells with partially undefined edges. Pattern Recognit Image Anal 18:112–7.

Sayeed MA, Ayesha N, Sayeed MA (2020). Detecting Crows on Sowed Crop Fields using Simplistic Image processing Techniques by Open CV in comparison with TensorFlow Image Detection API. Int J Res Appl Sci Eng Technol 8:61–73.

She FH, Tung KL, Kong LX (2008). Calculation of effective pore diameters in porous filtration membranes with image analysis. Robot Cim-Int Manuf 24:427–34.

Synopsys, Inc. (2024). Simpleware ScanIP. Sunnyvale, USA. https://www.synopsys.com.

Teo LL, Sagar BSD (2006). Modeling, description, and characterization of fractal pore via mathematical morphology. Discret Dyn Nat Soc 2006:089280.

Zhang Z, Su X, Ding L, Wang Y, et al (2013). Multi-scale image segmentation of coal piles on a belt based on the Hessian matrix. Particuology 11:549–55.

Zhang H, Dong Y, Li J, Xu D (2021). An efficient method for time series similarity search using binary code representation and hamming distance. Intell Data Anal 25:439–61.